Wireless OTFS-Based Integrated Sensing and Communication for Moving Vehicle Detection
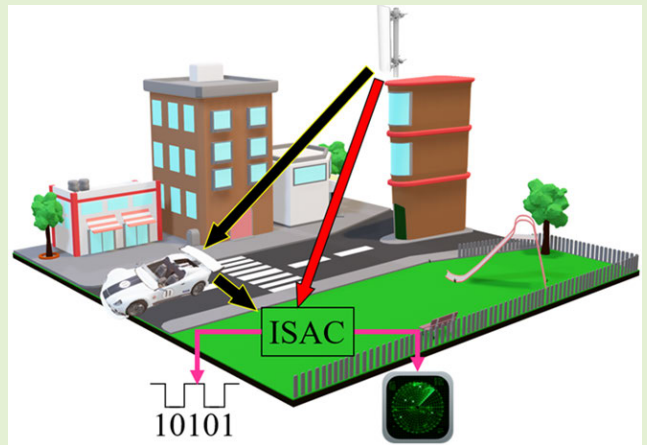
Tomasz P. Zieliński, Pavel Karpovich, Karol Abratkiewicz, *Member, IEEE*, Radosław Maksymiuk, Piotr Samczyński, *Senior Member, IEEE*, Krzysztof Duda, and Marek Wypich

Abstract—This article presents an approach for joint radar sensing and communications based on the orthogonal time–frequency space (OTFS) modulation, applied to a moving target detection during regular digital wireless transmission (TX). Most communication systems estimate and correct channel influence using specially designed reference signals or pilots. Pilots are usually known to the receiver before the TX, and the receiver estimates the channel impulse response (CIR) by analyzing the input (pilots) and output of the channel. Because of the Doppler effect, the movement of reflection sources (or targets in radar terminology) in multipath channels causes oscillations of CIR coefficients. Based on the frequency analysis of time-varying CIR, one can extract the distances and velocities of moving targets when the data is transmitted through the wireless channel. This article describes the application of OTFS with random pilots using both simulations and real-life field tests. It is shown that applied time-varying CIR estimation based on random pilot signals overcomes the OTFS with zero padding during vehicle velocity estimation in very noisy conditions. The proposed OTFS-based sensing method with the CIR-based channel estimation and vehicle detection is experimentally compared with the cross-ambiguity function (CAF) approach commonly used in radars. A thorough analysis shows that the proposed CIR-based approach outperforms the classical CAF-based radar processing in terms of target detection. Finally, the proposed integrated sensing and communication (ISAC) concept, including bit TX, is experimentally verified.

Index Terms—Channel impulse response (CIR), cross-ambiguity function (CAF), integrated sensing and communication (ISAC), moving vehicle detection, orthogonal time–frequency space (OTFS).

Tomasz P. Zieliński is with the Institute of Telecommunications, AGH University of Krakow, 30-059 Kraków, Poland (e-mail: tomasz.zielinski@agh.edu.pl).

Pavel Karpovich is with the Institute of Telecommunications, AGH University of Krakow, 30-059 Kraków, Poland, and also with Nokia Solutions and Networks, 30-348 Kraków, Poland.

Karol Abratkiewicz, Radosław Maksymiuk, and Piotr Samczyński are with the Institute of Electronic Systems, Warsaw University of Technology, 00-665 Warsaw, Poland.

Krzysztof Duda is with the Department of Measurement and Electronics, AGH University of Krakow, 30-059 Kraków, Poland.

Marek Wypich is with the Institute of Telecommunications, AGH University of Krakow, 30-059 Kraków, Poland, and also with Ericsson POL, 30-392 Kraków, Poland.

Digital Object Identifier 10.1109/JSEN.2024.3350238

I. INTRODUCTION

DUE to evolving new technologies and new application scenarios, like autonomous vehicles, smart industry, smart city, and so on [1], [2], integrated sensing and communication (ISAC) systems [3], [4], [5], [6], [7], [8], [9], [10] are becoming increasingly more important. The orthogonal frequency division multiplexing (OFDM) waveform is a data transmission (TX) method used in many high-mobility environments, but it has the disadvantage of being sensitive to the Doppler shift [11]. Consequently, current research efforts are focused on developing a successor method. The orthogonal time–frequency space (OTFS) modulation, introduced recently [12], [13], [14], [15], [16], [17], [18], is treated by many researchers as a promising candidate for future ISAC systems.

The classical vehicle detection approach used in active radar systems [19] is based on searching signal echoes indicated by maxima of output from matched filtering of the received waveform. In passive sensing [20], also known as passive coherent location (PCL), the reference signal is reconstructed entirely or partly from the reference antenna pointed directly toward the transmitter [e.g., digital radio or digital television (TV) transmitters, or digital audio broadcasting (DAB) and digital

video broadcasting-terrestrial (DVB-T)]. This reference signal is used for searching for the presence of the Doppler echoes in the signal from the surveillance antenna looking toward the area of interest. Target detection in such radars is usually done by the cross-ambiguity function (CAF) application.

On the other hand, any wireless communication system must estimate a channel impulse response (CIR) or a channel frequency response (CFR)—the discrete Fourier transform (DFT) of the CIR—to correct the channel influence upon the transmitted data. The CIR is characterized by coefficients describing signal TX paths and parameters of the signal echoes. It is possible to extract information about the distances and velocities of targets that reflect the signal from the CIR taps. Therefore, modern telecommunication systems solve tasks typical for sensing but in many applications do not exploit results from this analysis for the identification/characterization of an environment around a receiver. However, in the automotive industry, OFDM-based radars are used. For example, they were proposed in [21], used in vehicular applications [22], deeply analyzed in [23], optimized for high performance in [24], and recently discussed as a candidate method to be used in beyond 5G standards [8], [9], [10]. Indeed, Abdallah et al. [25] have recently investigated the utilization of frequency analysis of on-demand 5G downlink signals for navigation.

Recently, we have tested (via simulation) a CIR-based passive radar-on-demand concept exploiting the 5G cellular network [26]. This article shows how to: 1) apply the known method of time-varying CIR estimation and target detection used in the OFDM-based automotive data TX systems (described in [21], [22], [23], and [24]) to the modern OTFS-based ones, which offer more robust bit TX in high-mobility scenarios, for example, for high-speed trains and 2) build in this way a covert low-energy passive radar that does not exploit CAF. The CIR-based radar idea is applied to an OTFS-based communication system with random pilot (or random padding) signals (RP-OTFS), as proposed recently in [27] and [28]. Such a solution is more beneficial than using the OTFS with pilots exploiting zero-padding (ZP-OTFS) [14] because the random pilot has more energy and is more noise-immune. The proposed idea of CIR-based radar sensing using the OTFS system with random pilot signals is new and is not treated in OTFS-based radar literature [27], [28], [29], [30], [31], [32], [33].

The novelty of this article can be summarized as follows.

1) A new CIR-based target detection (including target range and velocity estimation) using the OTFS with random pilot signals is proposed and validated in simulations and real-life tests.
2) It is demonstrated that such a solution is more immune to strong noise than the OTFS signal with zero-padded pilots.
3) A whole OTFS system for joint sensing and communication using this new concept was designed in software-defined radio (SDR) technology and experimentally tested.
4) Successful data TX and target detection experiments confirm the possibility of joint communication and sensing using the proposed CIR-based OTFS method with random pilots.
5) Finally, it is shown that using OTFS waveforms with random pilots is not only capable of bit TX, but also allows

moving vehicle detection comparable to or better than classical CAF-based radar using the same waveform.

This article has the following structure. Section II presents the concept of the Rayleigh fading channel. Section III describes the OTFS technique used in this work and its ability to transmit data and target detection simultaneously for modern ISAC systems. Section IV is devoted to communication and sensing results obtained in simulations and field tests. This article is concluded in Section V.

II. RAYLEIGH FADING CHANNEL AND ITS ESTIMATION

A mobile Rayleigh fading channel with L Doppler reflections $l = 1, \ldots, L$ is described by the following input–output relationship (see [21], [22], [23], [24], [25]):

$$y(n) = \sum_{l=1}^{L} g_l x(n - n_l) e^{j 2\pi f_l^{(D)}(n\Delta_t)} \tag{1}$$

where $x(n)$, $y(n)$ are the samples of input (transmitted) and output (received) signals, respectively, n is the sample number (time index), g_l is the complex-value attenuation, n_l is the shifts of $x(n)$ in the number of sampling periods, which, in general, can also be fractional, $f_l^{(D)}$ is the Doppler frequency shifts of $x(n)$ in hertz, Δ_t is the sampling period in seconds, and $j = \sqrt{-1}$. Equation (1) can be rewritten into the following form:

$$y(n) = \sum_{l=1}^{L} h_l(n) x(n - n_l) \tag{2}$$

where

$$h_l(n) = g_l e^{j 2\pi f_l^{(D)}(n\Delta_t)}, \quad g_l = |g_l| e^{j \angle g_l}. \tag{3}$$

When a fading channel with zero Doppler ($f_l^{(D)} = 0$) or small Doppler ($f_l^{(D)} \approx 0$) effect is assumed, $h_l(n)$ reduces to g_l and $y(n)$ simplifies to

$$y(n) \approx \sum_{l=1}^{L} g_l x(n - n_l). \tag{4}$$

Assuming integer delays n_l, (4) can be written as a convolution

$$y(n) \approx \sum_{k=1}^{K} g(k) x(n - k) \tag{5}$$

where $g(k) = 0$ for most values of k. Since the convolution of the signals corresponds to the multiplication of their Fourier spectra, one can write $Y_n(f) = X_n(f) G_n(f)$, where $X_n(f)$ and $Y_n(f)$ denote short-time (local) Fourier spectra of fragments of signals $x(n)$ and $y(n)$, respectively, around sample index n for which coefficients $h_l(n)$ equal g_l. $G_n(f)$ is a channel frequency response, CFR, around time index n. The communication receiver has to estimate transmitted $X_n(f)$ having received $Y_n(f)$. Bit decoding is impossible without estimating and correcting the channel distortion. For this purpose, from time to time, the transmitter has to send a reference signal called a pilot (P), known to the receiver, with specified frequencies f_p. Knowing $X_n^{(P)}(f_p)$ and obtaining $Y_n^{(P)}(f_p)$, the receiver estimates,

in noisy conditions, a CFR valid for f_p around time n, for example, by

$$\hat{G}_n(f_p) = \frac{Y_n^{(P)}(f_p)}{X_n^{(P)}(f_p)}. \quad (6)$$

Then, the calculated $\hat{G}_n(f_p)$ is interpolated for all frequencies f_i of data carriers at the moment n and in between moments n and $n + K$, that is, inside intervals $[n, n + K]$. Calculated channel estimates $\hat{G}_{[n,n+K)}(f_i)$ are then used for correcting received data

$$\hat{X}_{[n,n+K)}(f_i) = \frac{Y_{[n,n+K)}(f_i)}{\hat{G}_{[n,n+K)}(f_i)}. \quad (7)$$

In the method presented, local Fourier spectra are computed for consecutive, nonoverlapping signal fragments. By performing the inverse Fourier transform (FT^{-1}) upon $\hat{G}_n(f_p)$ (6), estimates of instantaneous CIR coefficients g_k, used in (5), are found using

$$\hat{g}(k) = \text{FT}^{-1}(\hat{G}_n(f_p)) \quad (8)$$

which is valid for the moment n.

The communication channel estimation and correction operation are performed periodically upon signal samples' blocks. When a channel is time-varying due to the Doppler effect, one should use shorter blocks and repeat channel estimation and correction procedures more often to preserve the Nyquist limit. In this case, where the channel estimate is based on (6), (8) becomes more momentary and does not distort information about time-varying values of $h_l(n)$ [see (3)]. Therefore, harmonic oscillations can be observed in them for changing n. By performing the Fourier analysis of the lth CIR tap $h_l(n)$, one can find the Doppler shift associated with it. Additionally, by knowing the tap number, one can deduce the time delay (TD) of the analyzed signal reflection.

The analysis presented above leads to the definition of the CIR-based ISAC system shown in Fig. 1 that is already known in OFDM-based TX [21], [22], [23], [24]. But here, for the first time, the CIR-based ISAC approach is applied to the random-padded-OTFS (RP-OTFS)-based ISAC system [27], [28]. A pilot from the communication signal is initially used for channel estimation. Then, the results of the channel estimation stage are used for 1) channel equalization and bit recovery (communication task) and for 2) environment identification, that is, evaluation of the range-velocity (RV) map, of objects moving nearby (sensing/radar task).

Later in this article, the RV map term is used in the context of the sensing system, and a delay-Doppler (DD) grid term is used for the communication system. In fact, the RV map is a DD grid linearly scaled in both dimensions. Scaling factors recalculate sample indices to standard units (i.e., meters and meters per second). DD is more suitable for communication where a carrier number is used to identify the data or pilot carrier in the DD grid. The RV representation is more suitable for radars because the range and velocity of the target are their main focus.

III. ISAC SYSTEM WITH CIR-BASED SENSING

In this section, the concept of CIR estimation usage for channel sounding is applied for the first time to the random-padded OTFS-based communication system.
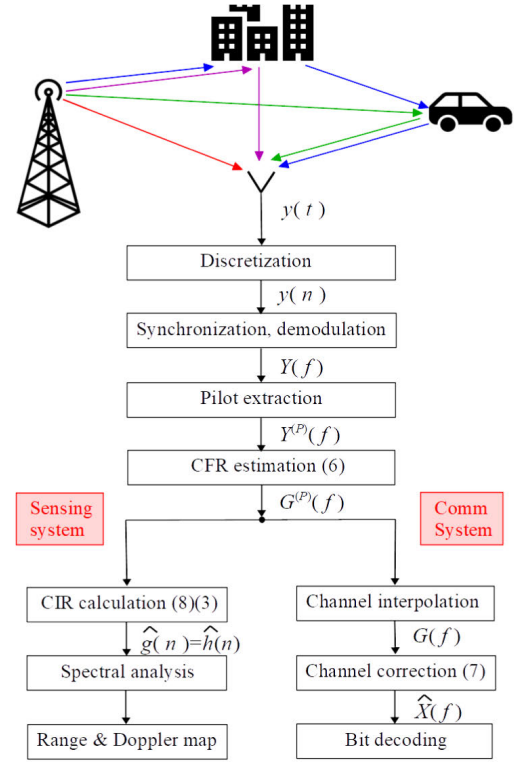

Fig. 1. Simulated and practically tested ISAC CIR-based system. Red arrow—direct transmitter–receiver signal; green arrow—signal reflected from a moving target; blue and violet arrows—multipath and clutter signals—reflections from stationary and very slow-moving targets.

TABLE I
PHYSICAL SENSE OF THE PARAMETERS M AND N IN DIFFERENT DOMAINS

Domain	M meaning	N meaning
TD	Decimation rate of a time domain signal $x(n)$ (Fig. 2)	Number of decimated signal samples
TF	Number of OFDM subcarriers	Number of OFDM symbols
DD	Number of delay taps	Number of Doppler taps

A. Basic Concept

The OFDM bits are coded in the time–frequency (TF) domain, and the OTFS bits are coded in the DD domain [34]. In both technologies, the TD matrix $\mathbf{X}$ is processed (see Fig. 2). However, in OTFS, $\mathbf{X}$ is built by *rows* that result from the inverse DFT (IDFT) computed over rows (Doppler axis) of the DD matrix $\mathbf{D}$. Whereas in OFDM, the matrix $\mathbf{X}$ is built by *columns* that result from IDFT computed over columns (frequency axis) of the TF matrix (the TF matrix is not shown in Fig. 2).

Both matrices $\mathbf{X}$ and $\mathbf{D} \in \mathbb{C}^{M \times N}$. Although from a mathematical perspective, M and N have the same meaning in all processing domains, they denote the number of rows and columns in $\mathbf{X}$ and $\mathbf{D}$. However, the physical sense of the parameters M and N depends on the domain where processing is carried out. In this article, three domains for analysis and processing are used: TD, TF, and DD. The physical meaning of the parameters is explained in Table I (also see Fig. 2) The choice of the particular M and N values depends on system requirements. Some considerations about choosing the parameters of the DD grid are given in [35].
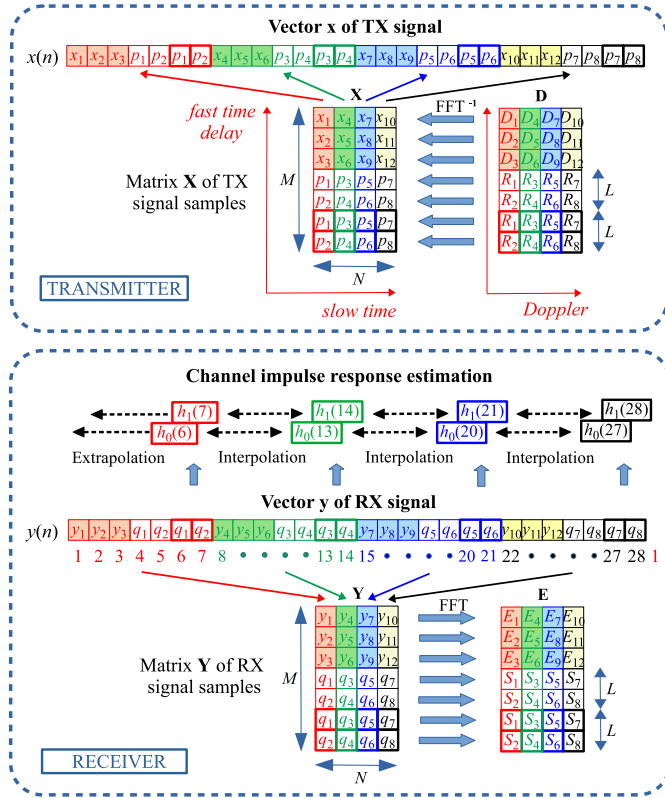
Fig. 2. Generation and TX of an RP-OTFS waveform (top), and its RX and decoding (bottom).

As in the case of OFDM, the elements D_k of the DD OTFS matrix $\mathbf{D}$ are complex-valued numbers with quadrature amplitude modulation (QAM), for example, 4-QAM, 16-QAM, having in-phase (I) real part and quadrature (Q) imaginary part that both carry data/bits. In turn, pilot samples R_k of the matrix $\mathbf{D}$ are chosen in such a way that IDFTs of the matrix $\mathbf{D}$ rows, built from R_k, give rows of the matrix $\mathbf{X}$ with pilot elements p_k, fulfilling the following, required condition: DFTs of columns of pilot samples, for example, $\{p_1, p_2\}, \{p_3, p_4\}, \{p_5, p_6\}, \ldots$, in Fig. 2, should give random complex-value numbers lying on the unitary circle. Thus, OFDM and OTFS are similar. However, OTFS has an advantage that each signal echo creates an attenuated, circular copy of the transmitted matrix $\mathbf{D}$, that is shifted in the delay axis (distance of the reflection source) and the Doppler axis (velocity of the reflection source). Therefore, the observed matrix $\mathbf{E}$ in the OTFS-based receiver (see Fig. 2) is equal to

$$E(n, k) = \sum_{l=1}^{L} g_l e^{j \frac{2\pi}{MN} k_l (n - n_l)} D(n - n_l, k - k_l). \quad (9)$$

For simplification in (9), integer time and integer Doppler frequency shifts are assumed to be given by

$$f_l^{(D)} = i_l \frac{1}{T} = i_l \frac{1}{(M \Delta_t) N}, \quad i_l = 0, 1, \ldots, N - 1. \quad (10)$$

For fractional values, sinc() functions are used for mathematical problem description, and 2-D interpolation methods should be exploited during the analysis of the DD matrix $\mathbf{E}$. Nevertheless, the relation (9) still approximately holds and can be used.

Because of the validity of (9), after synchronization and channel estimation based on transmitted pilots (i.e., finding parameters of each echo) [14], [37], it is possible to equalize the received data $\mathbf{E}$ and then to recover from it an estimation of the transmitted matrix $\mathbf{D}$ (see [38]). In comparison, the coded TF data matrix in OFDM is completely smeared in the presence of a high-value Doppler effect, and data recovery is very challenging in this case.

B. Channel Estimation in RP-OTFS Modulation

The RP-OTFS modulation has a dedicated pilot zone in matrices $\mathbf{X}$ and $\mathbf{D}$, hence the pilot information is not spread throughout the whole RP-OTFS frame in the time domain. It is concentrated in multiple short signal locations (see the vector of TX signal samples in Fig. 2, especially the elements marked with thick lines). In the receiver (see Fig. 2), one can use signal fragments with pilot samples only (drawn with bold borders again) and estimate channel coefficients $h_l(n)$—illustrated by arrows pointing up. The distance between pilot locations is M. The length of pilot blocks ($2 \times L$) is small, and one can assume that the CIR is stationary during this short time. In the receiver, one has to (see Fig. 2)

1) Find pilot samples q_k, that is, synchronize with them, which is not difficult since their values are known,
2) Skip the cyclic prefix of the pilot samples block, that is, the first pilot part, the length of the cyclic prefix should be longer than CIR to avoid interference coming from preceding samples with data and to keep the convolution circular,
3) Calculate the DFT of the second block of pilot samples,
4) Estimate the CIR, this could be done by any method used for channel estimation in the OFDM systems, for example, by one-tap equalizer—just by dividing the result of the previous step by the known DFT of transmitted pilot samples p_k, that is, practically exploiting (6),
5) Calculate the IDFT (8) to obtain $g_l(n)$ which represents $h_l(n)$,
6) Perform the SENSING TASK, that is, perform spectral analysis of $h_l(n)$ over n using any available frequency estimation method [39], for example, the Aboutanios-Ye iterative algorithm [40] or the interpolated DFT (IpDFT) method of Bertocco, Yoshida, or Bertocco-Yoshida [41],
7) Perform the COMMUNICATION TASK: interpolate $h_l(n)$ in remaining timestamps marked with dotted lines with arrows (in Fig. 2), that is, between pilot blocks, find $h_0(n), h_1(n), \ldots, h_{L-1}(n), n = 0, 1, \ldots, MN - 1$, perform equalization of received data samples $y(n)$, that is, extract elements D_k from E_k, and find transmitted bits, see [14], [38].

Steps 6) and 7) are joined together in the proposed approach, thereby allowing for simultaneous utilization of the received signal $y(t)$ for data TX and target detection using CIR analysis.

Since the pilots are known at the receiver, one can estimate the CIR. Furthermore, the estimates of the CIR are used by radar and communication systems. The communication system processing stages are straightforward. The radar system uses the estimates for detecting targets and estimating targets' parameters. This is a precious feature of the proposed method since the CIR-based approach uses only parts of the signal that

TABLE II
SIMULATION PARAMETERS

Parameter	Value	Description
Modulation	4-QAM	Type of carrier modulation
f_c	5.8 GHz	Carrier frequency
f_s	20 MSPS	Sampling rate
M	256	Number of samples in delay direction
N	64	Number of samples in Doppler direction
L	64	Number of pilot samples
N_{frames}	16, 32, 64, 128	Number of analysed frames

must be known to the transmitter and receiver to establish the connection. Thus, the superior nature of the method proposed in this work is that the sensing part is independent of the transmitted data, and the estimations of the CIR (which should be done regardless of the presence/absence of the radar system) carry information about signal propagation, reflection, and scattering. Thus, apart from communication, passive sensing (similar to passive radar) can be done using a cheap receiver without needing a dedicated antenna for the reference signal.

To avoid division by 0 in step 4), pilot elements R_k of the DD matrix **D**, shown in Fig. 2, have to be chosen as described before.

In summary, the RP-OTFS is similar to the ZP-OTFS described in detail in [14]. In the ZP-OTFS, the matrix **X** also consists of two parts: data (upper, the same as in the RP-OTFS) and pilot (lower, different than in the RP-OTFS). However, in the ZP-OTFS, each column of the pilot, lower submatrix has a form of unitary/impulse channel excitation $[\ldots, 0, 0, 0, 1, 0, 0, 0, \ldots]^T$ while in the RP-OTFS, a channel is identified by a pseudorandom sequence which is repeated twice: $[\mathbf{p}_k, \mathbf{p}_k]^T$. In other words, the channel estimation approach differs in these two methods. Since the pilot has significantly higher energy in the RP-OTFS than in the ZP-OTFS, one expects to obtain better noise immunity for the RP-OTFS during vehicle speed estimation in intense noise when an error part caused by noise is much higher than an error part originated in the RP-OTFS from using block-oriented DFT/IDFT signal processing for momentum CIR estimation. After replacing impulse excitation with a pseudorandom one, some modification of the channel correction procedure used in a communication part of the ZP-OTFS-based ISAC system has to be performed, but this issue is not addressed here. Some additional details concerning channel estimation and equalization performed in the discussed RP-OTFS ISAC system are given in [36].

IV. SENSING AND COMMUNICATION RESULTS

This section describes the results of simulations and field tests of the proposed sensing method. Only the new results from the sensing subsystem are presented: the results from the communication part, that is, bit error rate (BER) characteristics, are given in [27]. Parameters used in sensing simulation are the same as those used in SDR-based practical testing/verification and are defined in Table II. The communication and sensing scenario tested was illustrated in Fig. 1.

It is not guaranteed that reflections from the objects will fit precisely into the DD grid cells. In general, fractional delay and Doppler should be considered in the simulation. Fractional delay/Doppler will generate oscillations on the DD grid. But for wide-band systems with a reasonably high sample

rate, integer approximation for delays could be used without significant loss of accuracy. Also, such approximation could be used for Doppler frequency shifts, provided that N is high enough [14], [38]. In the presented simulation, the integer approximation was used only for delays.

A well-established and widely used CAF was chosen as a reference method. The CAF distribution as a function of velocity and delay is given as follows [19], [20]:

$$\Psi(R_b, V_b) = \int_0^{T_i} y(t)\hat{y}^*\left(t - \frac{R_b}{c}\right) \exp\left(-j\frac{2\pi}{\lambda} V_b t\right) dt \tag{11}$$

where $y(t)$ is the received signal (see Fig. 1), $\hat{y}(t)$ is its reconstruction [demodulated, decoded, and back-modulated $y(t)$], z^* denotes the complex conjugation of z, T_i is the integration time, R_b is the bistatic range, V_b is the bistatic velocity, and $\lambda = c/f_c$ is the wavelength. The results obtained with this method are used as the ground truth for further comparison.

A. Simulation of Low-Speed Vehicles

In the simulations, the OTFS frame consists of $MN = 16\,384$ samples and lasts 0.8192 ms. The signal fragment used for target frequency estimation is 128 times longer (approximately 105 ms). The Doppler shift was computed as $f_d = -V/\lambda$ (simplified bistatic Doppler shift [20]), where f_d is the Doppler frequency, $\lambda = c/f_c$ is the wavelength, c is the speed of light, and f_c is the carrier frequency.

To make the simulation scenario as similar as possible to the planned field tests, three near-field clutter echoes (signals reflected from stationary or very slow-moving targets) from the building were assumed (in the range of 0–50 m). The scenario also included several vehicles moving in the direction of the receiving (RX) antenna beam with randomly chosen velocity values (from 15 to 25 m/s) within a randomly chosen range (from 180 to 210 m for free objects moving toward the beam and from 225 to 245 m for three objects moving away from the antenna beam). Signal reflections from the vehicles were 100 times weaker than those from the clutter. It is important to mention that in the planned field experiment, the input signal-to-noise ratio (SNR), clutter with echoes to noise, was predicted to be around 10 dB. The simulations and the example of the presented results also assumed this SNR level. The transmitted signal $x(n)$ with random data and random pilots was sent through the described multipath channel, and white Gaussian noise (WGN) was added to the signal $y(n)$ obtained on the receiver input. For each SNR value, the simulation was repeated 625 times (for 25 different noise realizations for 25 different vehicle movements).

In Fig. 3, the example of simulation results are shown: superimposed discrete-time Fourier transform (DtFT) spectra of estimated CIR coefficients (upper) and the identical spectra plotted in the form of an RV map (lower).

Fig. 4 presents the root mean square error (RMSE) of velocity estimation, performed in the ISAC receiver sensing task (with no suppression of simulated clutter), from the Aboutanios-Ye iterative frequency analysis method [40] and three different interpolated DFT methods (Bertocco, Yoshida, and Bertocco-Yoshida order 1 [41]) as a function of the input SNR. Applied spectral analysis algorithms allow simultaneous
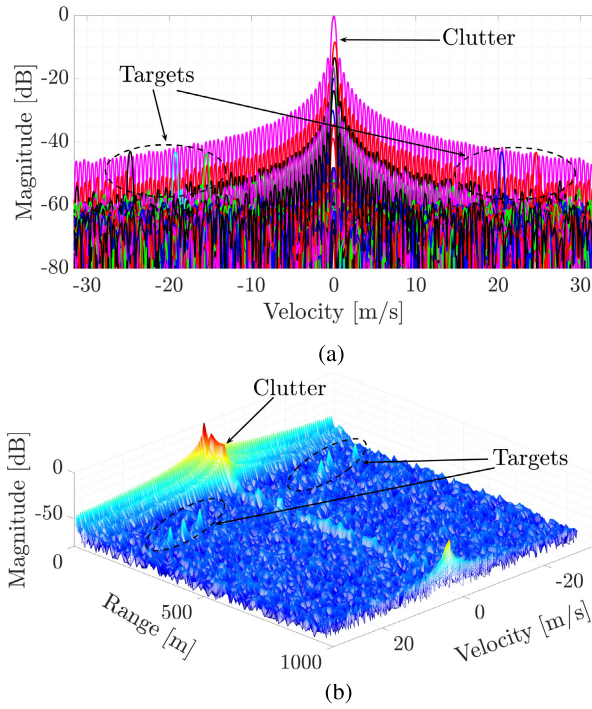
(a)

(b)

Fig. 3. Simulation results for vehicles moving with *low-speed* for SNR = 10 dB. (a) Superimposed DtFT spectra of all CIR coefficients. (b) Example of calculated RV map for many signal echoes.

estimation of many spectral peak positions. In the experiment, the Doppler shift for the bistatic case was used. Only $N_h = 128N = 8192$ samples of energetically dominant CIR taps resulting from signal echoes (and estimated in the receiver in 128 OTFS frames) were analyzed. The variance of frequency estimation of a complex value sinusoidal signal, embedded with given SNR in an additive WGN, is bounded by the Cramér–Rao lower bound (CRLB) given by [42]. After scaling to velocity, one gets

$$\text{CRLB}(v) = s \cdot \frac{6}{\eta N_h (N_h^2 - 1)}, \quad s = \left(\frac{N f_0}{f_c} c\right)^2 \left(\frac{1}{2\pi}\right)^2 \tag{12}$$

where $\eta = 10^{\text{SNR}/10}$. Fig. 4 depicts the RMSE of velocity estimation, based on the Doppler frequency shift, along with the lower band for its standard deviation [i.e., the square root of the CRLB(v)].

Applied frequency estimators are known for good statistical efficiency, yet obtained RMSEs diverge from the CRLB. This shows that the recovered CIR taps are slightly distorted and are not pure complex sinusoids, especially in the presence of Doppler shifts, which are fractional in relation to the OTFS sampling grid. Therefore, the observed RMSE curves suffer from the additive noise and the Doppler signal reconstruction error. The following conclusions can be drawn from Fig. 4, analyzing it using a top down approach.

1) The ZP-OTFS, a predecessor of the RP-OTFS, is more noise-sensitive due to the usage of pilot signals with many samples equal to zero, that is, due to its significantly lower energy.
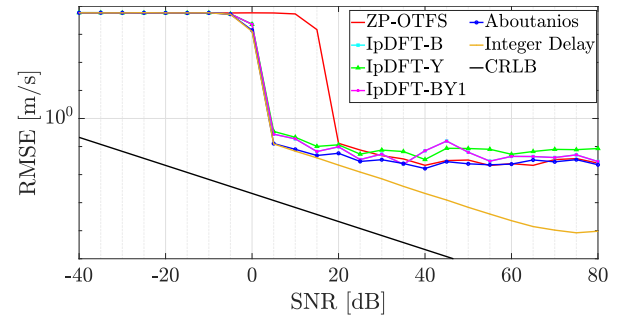2) The RP-OTFS is less noise-sensitive, and in the discussed configuration and environmental conditions,

Fig. 4. RMSE of estimated velocities of simulated vehicles moving with *low-speed* using iterative Aboutanios-Ye method [40] and some IpDFT algorithms [41]. CRLB denotes the Cramér–Rao lower bound [42]. The best results obtained for the OTFS with zero-padding [14] have been added for comparison and calculated only for the Aboutanios-Ye method.

it starts to work correctly beginning with the SNR equal to 5 dB, compared with 20 dB for the ZP-OTFS.

3) For fractional delays of echoes, stronger sidelobe oscillations are present and visible in RD maps; for this reason, the RMSE curves, both for ZP-OTFS and RP-OTFS, saturate at approximately 0.1–0.01 m/s.

4) For integer delays, the sidelobe oscillations are not visible in the RD maps, and for the high SNR, a linear dependency is observed, which is parallel to the CRLB line; however, for very high SNR values, the RMSE characteristics stop decreasing due to the estimation error of momentum CIR values employing a block-based DFT/IDFT approach—this effect is dominating at this point over the noise error.

5) Finally, the CRLB line is at the very bottom since it specifies the theoretical limit of pure harmonic frequency estimation in Gaussian noise.

Obtained results are promising and comparable to those presented in [30] for an OTFS-based radar working on different principles. They confirm the correctness and demonstrate the efficiency of the idea proposed in this article for sufficient (i.e., above 5 dB) input SNR.

For comparison in Fig. 4, results obtained for the original ZP-OTFS method [14] are also presented. As expected, they are worse for the low input SNR and better for very high SNR.

Since the results shown above were obtained without using any clutter removal algorithm when the clutter was present (see Fig. 3), they confirm some clutter robustness of the method. To check the benefits of clutter removal techniques, the simulations were repeated with the usage of an extensive clutter cancellation algorithm (ECA) [43], in its carrier and Doppler shift version (ECA-CD) [44] supported by an initial, additional clutter estimation [45]. Since only an incremental improvement was gained for the very low SNR (but at the price of a dramatic increase in calculation time), these results are not presented here.

Since system desynchronization causes a mismatch between estimated CIR taps and the RV map grid, the influence of synchronization error upon the generated clutter level was also simulated. It is presented in Fig. 5. As can be seen, time synchronization error has a more significant influence than frequency error on the generated clutter, that is, the CIR peak is 20 dB lower for a ±0.5 synchronization mismatch (while for perfect synchronization in time and in frequency,
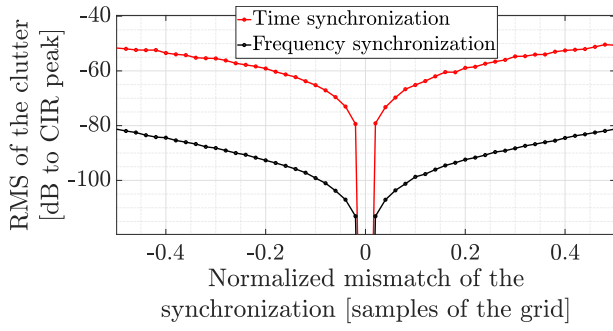
Fig. 5. Dependency of the clutter level on synchronization errors.

the CIR peak height is more than 120 dB). Additionally, observed clutter also results from the inconsistency of signal reflection parameters with the RV map grid (i.e., fractional delay and Doppler). Nevertheless, the clutter generated by the most robust signal path (more often, it is a line-of-sight path from the transmitter to the receiver) could be eliminated by good synchronization in the case of CIR-based radars.

B. Simulation of High-Speed Vehicles

To demonstrate that the proposed technique can also be used in high-mobility scenarios, the authors simulated six high-speed vehicles, for example, drones or airplanes, at random distances chosen from the range [120–840] m and with random velocities selected from the interval [50–150] m/s. As for the low-speed example, the simulation was repeated 625 times. Obtained results are presented in Figs. 6 and 7 and are very promising. Despite the big difference in vehicle velocities, the noise floor of the method is very similar in the DtFT spectra, and it is only slightly higher in the high-speed scenario compared with the low-speed one (compare Fig. 6 with Fig. 3). This indicates that the influence of the Doppler effect change upon CIR and velocity estimation (causing CIR coefficient oscillation as a result of signal reflections from moving objects) is not very severe. This observation is confirmed by RMSE = $f(\text{SNR}_{\text{input}})$ curves presented in Fig. 7, which are very similar to the ones in Fig. 4. However, the following differences can be observed.

1) Since distances between moving vehicles are significantly greater in the high-speed test than in the low-speed one, the sidelobe influence is much lower, and the RMSE saturation effect occurs for higher SNR (approximately >40 dB) than before.
2) Because of this effect in all RMSE curves, longer linear fragments are observed, both for fractional and integer delays.
3) The RMSE variability for very high SNR is now bigger since for higher velocities, the error caused by the block-based DFT/IDFT velocity estimation method is larger and dominating over the noise error; it is especially visible for the integer delay case, that is, for the bottom curve.

As seen in Fig. 6, in the high-speed scenario, clutter influence is less of a concern, and thus, it is not investigated below.

Fig. 8 depicts the output SNR as a function of the input SNR for simulated vehicle speed (v_m) equal to 25 m/s (Fig. 3) and 150 m/s (Fig. 6), and the DtFT/DFT observation time (T_i)
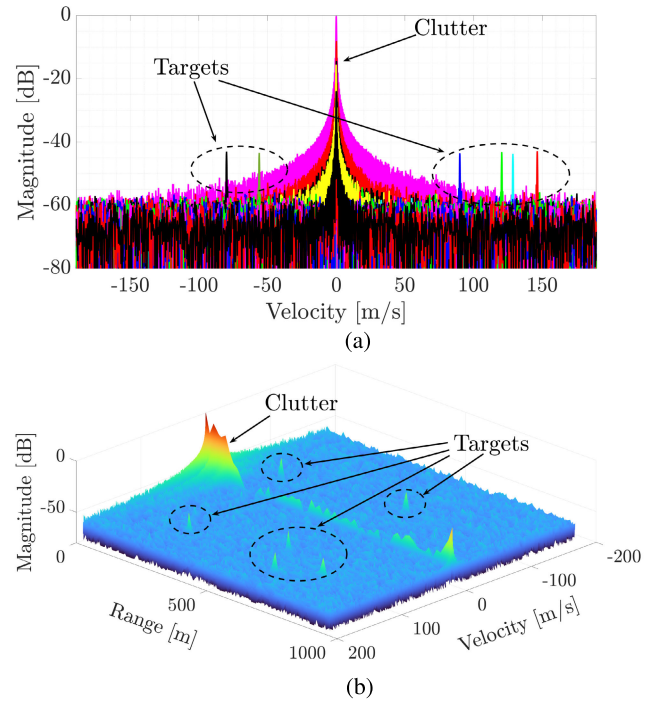

Fig. 6. Simulation results for vehicles moving with *high-speed* for SNR = 10 dB. (a) Superimposed DtFT spectra of all CIR coefficients. (b) Example of calculated RV map for many signal echoes.
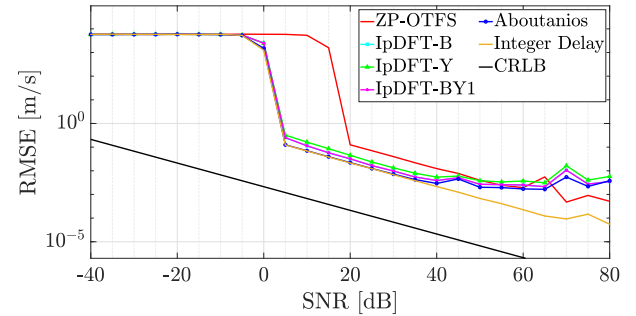

Fig. 7. RMSE of estimated velocities of simulated vehicles moving with *high-speed* using iterative Aboutanios-Ye method [40] and some IpDFT algorithms [41]. CRLB denotes the Cramer–Rao lower bound [42]. The best results obtained for the OTFS with zero-padding [14] were added for comparison and calculated only for the Aboutanios-Ye method.

value equal to 10, 100, and 200 ms. Simulation results for both, CAF and CIR, methods are shown. The output SNR was defined as follows:

$$\text{SNR}_{\text{out}}(l) = 20 \log_{10}\left(\frac{A_{\text{echo}}(l)}{\text{rms}\{A_{(\text{noise})}(k)\}}\right)[\text{dB}] \qquad (13)$$

where $A(\cdot)$ denotes the magnitude of the calculated RV map, $A_{\text{echo}}(l), l = 1, 2, \ldots, L$, is the magnitude of the lth $A(\cdot)$ peak corresponding to the echo (moving target) in question, $A_{\text{noise}}(k), k = 1, 2, \ldots, K$, is the magnitude of the kth element of the $A(\cdot)$ region where no target was present, and rms$\{\cdot\}$ denotes the root mean square value. For example, in both Figs. 3 and 6, one can see six small peaks of moving vehicles having $\text{SNR}_{\text{out}}(l), l = 1, 2, \ldots, 6$, approximately equal to 20 dB and this is their relative height above the noise floor. The difference in the output SNR between Figs. 3 and 8 or 6 is due to the absence of the zero-Doppler clutter in Fig. 8,
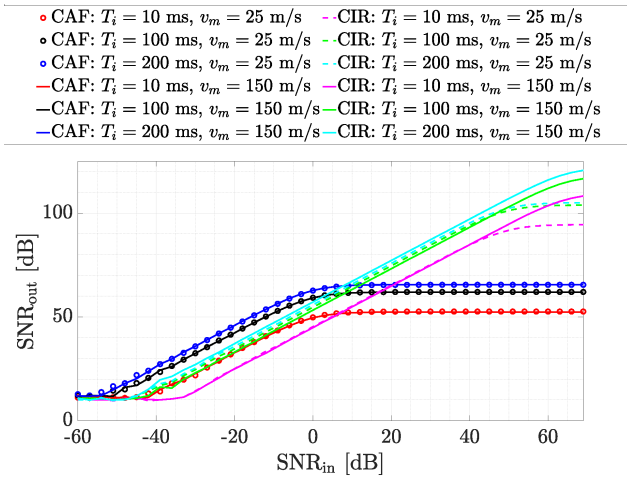

Fig. 8. Output SNR, that is, the relative height of the detection peak, in CIR-based RP-OTFS radar as a function of input signal SNR, for different DFT length (T_i in ms) and different vehicle speed (v_m in m/s).
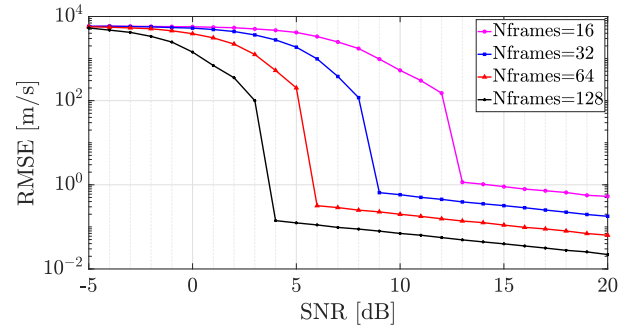

Fig. 9. RMSE of estimated vehicle velocities for Aboutanios-Ye method [40] and a different number of OTFS frames used for spectral analysis of CIR taps.

where one estimates the maximum achievable performance. Also, in the case of CIR, it can be seen in Fig. 8 that up to input SNR = 50 dB vehicle velocity value does not affect the result. For higher input SNRs, the output SNR curve saturation is observed for high-speed objects due to the increasing influence of the accuracy of the CIR estimation. Increasing the CIR observation time and DFT length leads to increased detection peak heights, and consequently, errors in the velocity estimation are no longer hidden by noise. The errors result from the assumption of the CIR being constant during the short-time pilots. As a consequence, RMSE velocity curves, presented in Figs. 4 and 7, shift slightly down when the DFT length is increased, which was observed but is not presented here.

In the case of CAF-based signal processing, the situation observed in Fig. 8 is different. For CAF, the output SNR curves become saturated for significantly lower input SNR than for CIR, for example, for 0 dB instead of 50 dB. Moreover, the origin of this saturation is also different. In the case of the CAF-based method, the primary limiting factors are the sidelobes of the ambiguity function of the RP-OTFS waveform: when an input signal is too weak, the CAF sidelobes are hidden in the noise, while for stronger input signals with higher SNRs, they are visible and they limit the sensing performance. From Fig. 8, we can also conclude that as follows.

1) The performance of the CAF method strongly depends upon the integration time and it does not depend on the speed of a target.
2) For input SNR lower than 0 dB, the CAF method offers higher output SNR due to the usage of all signal samples for sensing (on the contrary, in the CIR method, only pilot samples are exploited, in our example, only 25% of all samples).

In comparing Figs. 7 and 8, it is noted that in Fig. 7, the RMSE curves descend, but in Fig. 8, the SNR_out curves ascend, starting at some different SNR values of the input/analyzed signal (for different SNR_in values). This effect is caused by clutter missing in the experiment reported in Fig. 8.

Finally, the authors investigated the high-mobility scenario of how velocity RMSE curves depend on the number of OTFS frames used for spectral analysis of CIR taps. Since the Aboutanios-Ye method was the best among the four frequency estimation algorithms tested, only results for this method are shown in Fig. 9. It is seen, as expected, that the shorter the analysis time is, the higher the method sensitivity to noise is, and the higher the input SNR that is required for method application.

C. Field Tests

The trials aimed to experimentally verify the proposed CIR-based approach to joint communication and sensing using the OTFS signal. During the experiment, both systems' features were examined. Namely, the signal was transmitted as in a classical wireless system to exchange the data between the transmitter and the receiver, and simultaneously, the CIR was calculated, allowing a moving target to be detected.

The tests were carried out at the campus of the Warsaw University of Technology, Warsaw, Poland. The measurement geometry can be seen in Fig. 10. The transmitter and the receiver consisted of a National Instruments USRP 2953R SDR equipped with two UBX-160 daughterboards and were synchronized through the GPS-disciplined oscillator. The transmitter was placed around 20 m above ground level, ensuring illumination of the area under interest (road). The receiver was placed in the parking lot at a range of about 50 m from the transmitter in the illuminated sector. The transmitter–target range was approximately 180 m, and the target–receiver range was approximately 110 m. The total bistatic range [20] can be assumed to be 240 m. The emulated transmitter generated the signal using values given in Table II. Then, the signal was passed to a high-power amplifier and transmitted by an antenna with a beamwidth of approximately 16° in both azimuth and horizontal dimensions and a directivity of about 19 dBi. The ISAC receiver acquired the signal after passing through a set of low-noise amplifiers and bandpass filters between the antenna and the SDR. The amplifier gain was 20 dB.

In a typical passive radar, usually, a two-channel receiver is used. The first is connected to the antenna pointed toward the signal source (to receive the reference signal), and the second observes the area of interest [20]. However, if the signal structure is known, the waveform can be reconstructed (demodulated, decoded, and then back-modulated to obtain a signal void of noise and reflection) and compared (correlated)
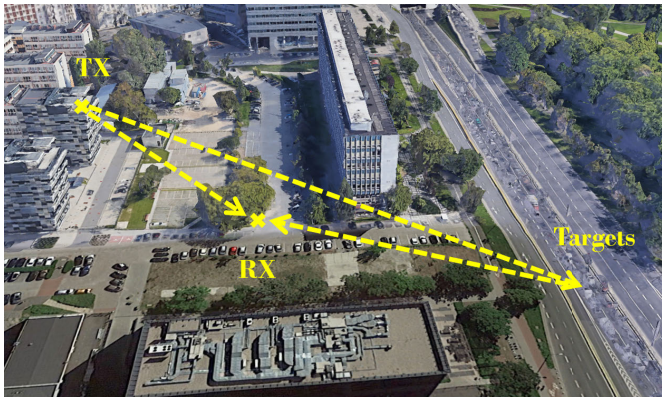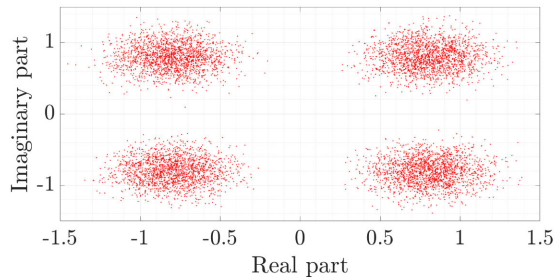
Fig. 10. Setup of the ISAC experiment.

Fig. 11. Observed IQ constellation of data carrier states.

with the received one. The single-antenna approach is known in passive sensing and reduces a system cost by removing one channel (on the other hand, the computational cost increases since the signal has to be resynthesized) [46]. The signal reflected from moving cars reached the receiver and was digitized, stored, and processed offline.

The recorded signal allowed target detection using a single-antenna system's proposed channel estimation technique. At first, the signal was synchronized, demodulated, and decoded. The example of the observed constellation of carrier states is shown in Fig. 11. As illustrated, the signal's IQ data distribution exhibits the 4-QAM modulation type used in the experiment for digital data TX. The BER was 0.06 because there is no line-of-sight path in this case, and the TX path was not stable (in Fig. 11, results are presented for the moment when the path was stable). The second system's task, namely moving target detection, was performed in the next step. The RV maps without and after ECA-CD-based clutter removal [44] depicted in Fig. 12(a) and (b) were obtained based on spectral analysis of calculated $128N = 8192$ samples per one CIR tap (128 frames with $N = 64$ samples) using the algorithm described in this work. As can be seen, a moving target in the range of 240 m with a velocity of approximately 7.24 m/s is apparent (from applying the Aboutanios-Ye method, the value 7.206 m/s was obtained, although the true data is unknown since real-world traffic was monitored). The echo originates from cars moving on the road, as the ISAC system observes. Additionally, a few more targets can be seen in the range of 50 m, resulting from traffic at the illuminated parking lot. The detection results coincide with the outcomes obtained using the classical bistatic radar processing based on the CAF calculation. In the experiment, the integration time was 105 ms, which corresponds to the signal length used in
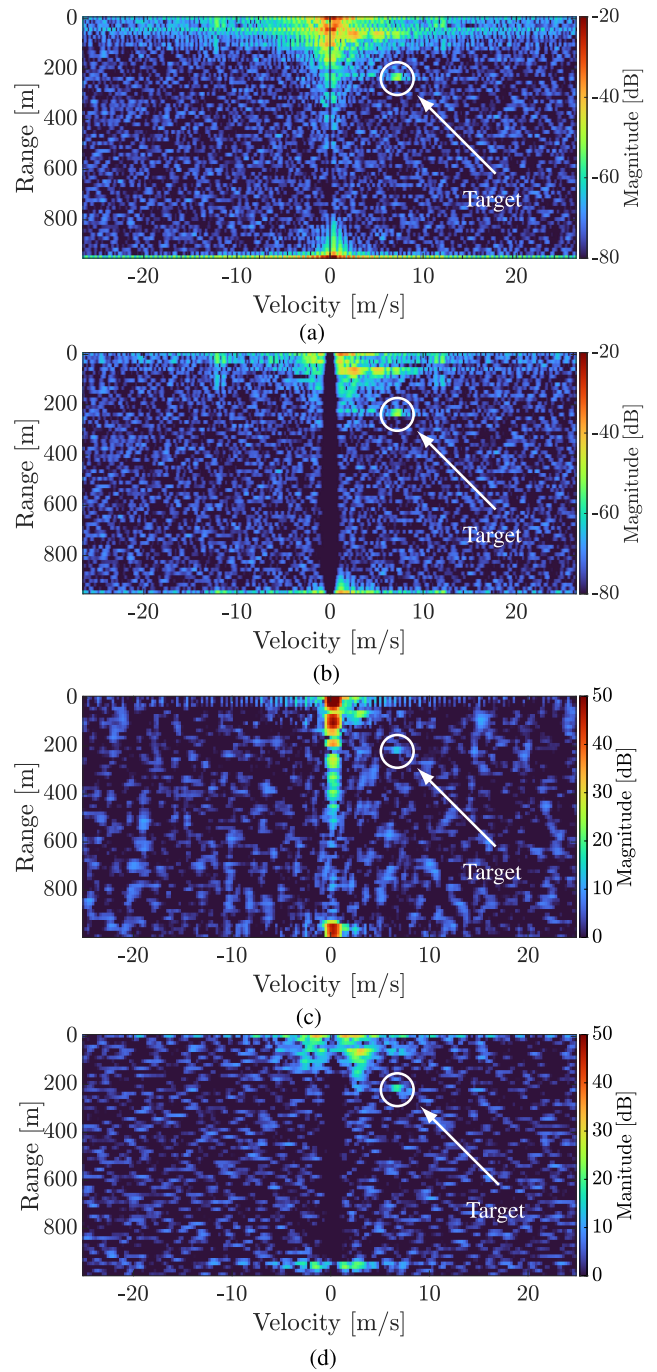

Fig. 12. Measurement results. The target (car) visible at $R_b = 240$ m and $V_b = 7.24$ m/s. (a) RV map obtained from CIR without clutter filtering. (b) RV map obtained from CIR after clutter filtering. (c) RV map obtained from CAF without clutter filtering. (d) RV map obtained from CAF after clutter filtering.

the CIR-based method. The results of the CAF-based radar processing are shown in Fig. 12(c) and (d) (before and after additional clutter filtering using a lattice filter, respectively) and exhibit cohesion with Fig. 12(b) as both allow for target detection at the same range and velocity. The results confirmed the proposed method's usability and correctness in two ways. For the DtFT-based method, the output SNR value of the detection peak equals 27.8 dB, and in the reference CAF-based method, 18.6 dB. So, the proposed approach outperforms the classical one.
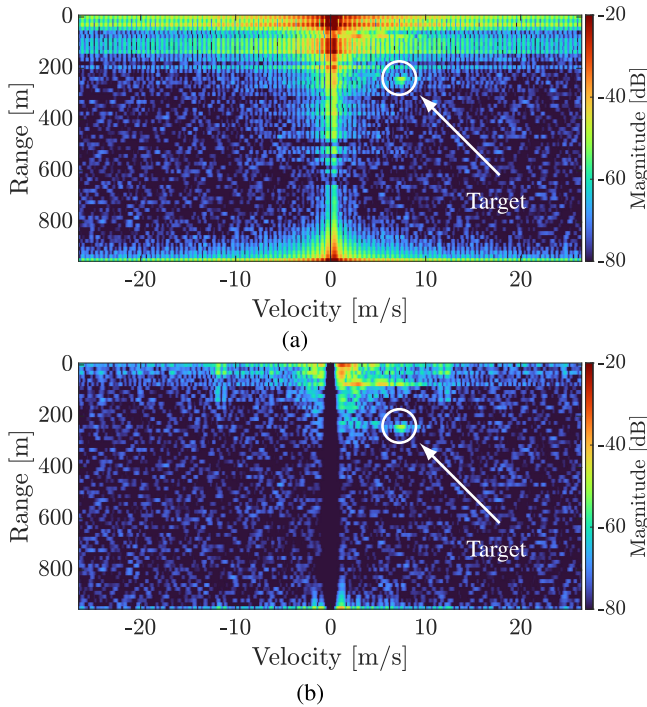
Fig. 13. Measurement results obtained for large time and frequency synchronization errors. (a) RV map without ECA clutter removal. (b) RV map with ECA clutter removal.

The consequences of wrong TF synchronization in the CIR-based radar are shown in Fig. 13. Before further processing, the received signal was first shifted relative to the RV sampling grid, that is, in time and frequency. As observed in the top image, the signal desynchronization concerning the RV grid results in severe smearing of the RV map, especially in regions with strong clutter components [compare Fig. 13(a) with Fig. 12(a)]. However, the application of the ECA-CD clutter cancellation algorithm [44] can remedy this problem, as presented in the bottom image.

Finally, Fig. 14 compares the variation of the output SNR with integration time for two tested methods. The outcomes clearly show that the CIR method outperforms the CAF method in our field test and that the detection peak becomes higher for both methods with longer integration. This is in agreement with the simulation results shown in Fig. 8: increasing the number of analyzed frames, that is, the FFT length, leads to increasing SNR_{out} for $SNR_{in} = 10$ dB, a value observed in our field test.

A further observation is that for the CAF-based approach, clutter removal improves the detection quality as the target echo becomes higher when the noise floor is suppressed. Both conclusions are in line with expectations. In turn, for the proposed CIR-based approach, the clutter filtering does not essentially leverage detection performance, and its detection peak is higher when the system is precisely synchronized. This means that for this method, clutter removal can be neglected (assuming that very slow targets are not observed). What is very important is that the CIR-based method is characterized by a higher echo peak, allowing for easier detection even without clutter removal. Second, comparing the proposed (CIR-based) approach and the CAF-based, their output SNR differs by at least 12 dB (for nonclutter removal processing). The difference is lower, however, but still meaningful after
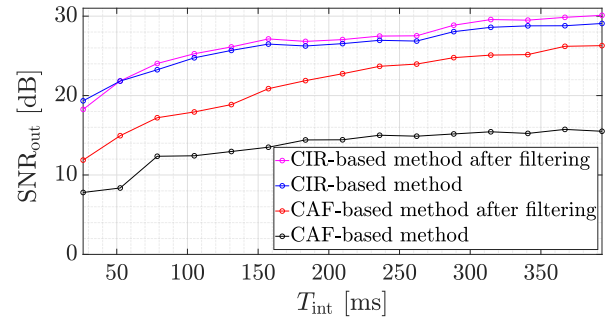

Fig. 14. Comparison of the output SNR peak versus integration time of two analyzed methods.

the CAF-based technique with clutter suppression. It has to be kept in mind that during the processing, for higher integration times, the target occupied two RV cells; thus, the total echo energy was spread, influencing the output SNR curves in Fig. 14. Mitigating this effect in the CIR-based approach will be the topic for further research.

V. CONCLUDING REMARKS

It has been shown in this article that results from the channel estimation, performed in communications receivers using the random padded OTFS, can be successfully used for finding distances and velocities of moving targets (ground-moving vehicles—cars, trucks, buses, but potentially also flying targets). In the proposed method, first, the coefficients of CIR are estimated, similar to the OFDM-based systems, and second, their spectral analysis over a long time period is performed. The joint communication and sensing system capability was experimentally validated using the proposed approach and confirmed the possibility of simultaneous data TX and moving target detection. It was demonstrated that the random padded OTFS-based ISAC system offers a smaller velocity estimation error than the zero-padded one. It was shown in simulation and real-life experiments that CIR-based moving target detection can be done even without clutter suppression if system synchronization is precise enough. This is unlike the CAF-based method, where clutter suppression is obligatory. It should be especially stressed that in the proposed approach, the target is defined by the higher SNR even when the clutter is not removed. Nevertheless, a deeper analysis of the clutter influence and its removal will be the main direction of the authors' future research.

Since the OTFS is currently considered superior over the OFDM in high-mobility communication scenarios, it is essential to know that OTFS-based receivers can also be used for sensing purposes. The proposed method is generally helpful in systems when the signal cannot be fully reconstructed (e.g., 5G) and complete passive radar processing cannot be performed in the receiver. Also, because of the way a single antenna operates, the method can be used in lightweight, flexible sensors, and communication terminals with low computational power.

REFERENCES

[1] *5G; Study on Scenarios and Requirements for Next Generation Access Technologies*, document TR 38.913, Version 17, ETSI, 3GPP, May 2022.

[2] M. Noor-A-Rahim et al., "6G for vehicle-to-everything (V2X) communications: Enabling technologies, challenges, and opportunities," *Proc. IEEE*, vol. 110, no. 6, pp. 712–734, Jun. 2022.

[3] M. Bekar, C. J. Baker, E. G. Hoare, and M. Gashinova, "Joint MIMO radar and communication system using a PSK-LFM waveform with TDM and CDM approaches," *IEEE Sensors J.*, vol. 21, no. 5, pp. 6115–6124, Mar. 2021, doi: 10.1109/JSEN.2020.3043085.

[4] D. Garmatyuk, J. Schuerger, and K. Kauffman, "Multifunctional software-defined radar sensor and data communication system," *IEEE Sensors J.*, vol. 11, no. 1, pp. 99–106, Jan. 2011, doi: 10.1109/JSEN.2010.2052100.

[5] S. D. Blunt and E. S. Perrin, Eds., *Radar and Communication Spectrum Sharing* (Electromagnetics and Radar). Edison, NJ, USA: IET, 2018. [Online]. Available: https://shop.theiet.org/radar-communi-spectrum-1e

[6] J. A. Zhang et al., "An overview of signal processing techniques for joint communication and radar sensing," *IEEE J. Sel. Topics Signal Process.*, vol. 15, no. 6, pp. 1295–1315, Nov. 2021.

[7] J. A. Zhang et al., "Enabling joint communication and radar sensing in mobile networks—A survey," *IEEE Commun. Surveys Tuts.*, vol. 24, no. 1, pp. 306–345, 1st Quart., 2022.

[8] T. Wild, V. Braun, and H. Viswanathan, "Joint design of communication and sensing for beyond 5G and 6G systems," *IEEE Access*, vol. 9, pp. 30845–30857, 2021.

[9] F. Liu et al., "Integrated sensing and communications: Toward dual-functional wireless networks for 6G and beyond," *IEEE J. Sel. Areas Commun.*, vol. 40, no. 6, pp. 1728–1767, Jun. 2022.

[10] Z. Wei et al., "Integrated sensing and communication signals towards 5G-A and 6G: A survey," *IEEE Internet Things J.*, vol. 10, no. 13, pp. 11068–11092, Jul. 2023.

[11] T. Wang, J. G. Proakis, E. Masry, and J. R. Zeidler, "Performance degradation of OFDM systems due to Doppler spreading," *IEEE Trans. Wireless Commun.*, vol. 5, no. 6, pp. 1422–1432, Jun. 2006.

[12] Z. Wei et al., "Orthogonal time-frequency space modulation: A promising next-generation waveform," *IEEE Wireless Commun.*, vol. 28, no. 4, pp. 136–144, Aug. 2021.

[13] S. S. Das and R. Prasad, *Orthogonal Time Frequency Space Modulation: OTFS a Waveform for 6G*. Denmark, Europe: River Publishers, 2021.

[14] Y. Hong, T. Thaj, and E. Viterbo, *Delay-Doppler Communications: Principles and Applications*. New York, NY, USA: Academic Press, 2022.

[15] R. Hadani et al., "Orthogonal time frequency space modulation," 2018, *arXiv:1808.00519*.

[16] S. K. Mohammed, "Derivation of OTFS modulation from first principles," *IEEE Trans. Veh. Technol.*, vol. 70, no. 8, pp. 7619–7636, Aug. 2021.

[17] C. Liu, S. Liu, Z. Mao, Y. Huang, and H. Wang, "Low-complexity parameter learning for OTFS modulation based automotive radar," in *Proc. IEEE Int. Conf. Acoust., Speech Signal Process. (ICASSP)*, Toronto, ON, Canada, Jun. 2021, pp. 8208–8212, doi: 10.1109/ICASSP39728.2021.9414107.

[18] Z. Gong, S. Liu, and Y. Huang, "Doppler diversity reception for OTFS modulation," in *Proc. IEEE 95th Veh. Technol. Conf. (VTC-Spring)*, Helsinki, Finland, Jun. 2022, pp. 1–5, doi: 10.1109/VTC2022-Spring54318.2022.9860675.

[19] M. A. Richards, *Fundamentals of Radar Signal Processing*. New York, NY, USA: McGraw-Hill, 2014.

[20] M. Malanowski, *Signal Processing for Passive Bistatic Radar*. Norwood, MA, USA: Artech House, 2019.

[21] C. Sturm, E. Pancera, T. Zwick, and W. Wiesbeck, "A novel approach to OFDM radar processing," in *Proc. IEEE Radar Conf.*, May 2009, pp. 1–4.

[22] M. Braun, C. Sturm, A. Niethammer, and F. K. Jondral, "Parametrization of joint OFDM-based radar and communication systems for vehicular applications," in *Proc. IEEE 20th Int. Symp. Pers., Indoor Mobile Radio Commun.*, Tokyo, Japan, Sep. 2009, pp. 3020–3024.

[23] C. Sturm and W. Wiesbeck, "Waveform design and signal processing aspects for fusion of wireless communications and radar sensing," *Proc. IEEE*, vol. 99, no. 7, pp. 1236–1259, Jul. 2011.

[24] G. Hakobyan and B. Yang, "High-performance automotive radar: A review of signal processing algorithms and modulation schemes," *IEEE Signal Process. Mag.*, vol. 36, no. 5, pp. 32–44, Sep. 2019.

[25] A. Abdallah, J. Khalife, and Z. M. Kassas, "Exploiting on-demand 5G downlink signals for opportunistic navigation," *IEEE Signal Process. Lett.*, vol. 30, pp. 389–393, 2023.

[26] M. Wypich and T. P. Zielinski, "5G NR based radar-on-demand using channel impulse response estimate," in *Proc. Signal Process. Symp. (SPSympo)*, Sep. 2023, pp. 220–225.

[27] P. Karpovich and T. P. Zielinski, "Random-padded OTFS modulation for joint communication and radar/sensing systems," in *Proc. 23rd Int. Radar Symp. (IRS)*, Sep. 2022, pp. 104–109.

[28] P. Karpovich, T. P. Zielinski, R. Maksymiuk, P. Samczyński, K. Abratkiewicz, and P. Tomikowski, "Field tests of a random-padded OTFSM waveform in a joint sensing and communication system," in *Proc. IEEE Int. Conf. Commun. (ICC)*, May 2023, pp. 1–7.

[29] P. Raviteja, K. T. Phan, Y. Hong, and E. Viterbo, "Orthogonal time frequency space (OTFS) modulation based radar system," in *Proc. IEEE Radar Conf. (RadarConf)*, Apr. 2019, pp. 1–6.

[30] L. Gaudio, M. Kobayashi, G. Caire, and G. Colavolpe, "On the effectiveness of OTFS for joint radar parameter estimation and communication," *IEEE Trans. Wireless Commun.*, vol. 19, no. 9, pp. 5951–5965, Sep. 2020.

[31] M. F. Keskin, H. Wymeersch, and A. Alvarado, "Radar sensing with OTFS: Embracing ISI and ICI to surpass the ambiguity barrier," in *Proc. IEEE Int. Conf. Commun. Workshops (ICC Workshops)*, Jun. 2021, pp. 1–6.

[32] A. S. Bondre and C. D. Richmond, "Dual-use of OTFS architecture for pulse Doppler radar processing," in *Proc. IEEE Radar Conf. (Radar-Conf)*, Mar. 2022, pp. 1–6.

[33] A. Correas-Serrano, N. Petrov, M. Gonzalez-Huici, and A. Yarovoy, "Comparison of radar receivers for OFDM and OTFS waveforms," in *Proc. 19th Eur. Radar Conf. (EuRAD)*, Sep. 2022, pp. 1–4.

[34] P. Karpovich and T. P. Zielinski, "Testing zero-padded OTFSM with additional pilot in high Doppler transmission scenarios," in *Proc. Signal Process., Algorithms, Architectures, Arrangements, Appl. (SPA)*, Sep. 2022, pp. 116–121.

[35] P. Karpovich and T. P. Zielinski, "Vehicle detection in 6G systems with OTFS modulation," in *Proc. Konferencja Radiokomunikacji Teleinformatyki*, Krakow, Poland, 2023, pp. 1–4.

[36] P. Karpovich and T. P. Zielinski, "Channel estimation and equalization in OTFS transmission system with random padding," in *Proc. Signal Process. Symp. (SPSympo)*, Poland, Europe, Sep. 2023, pp. 67–72.

[37] P. Raviteja, K. T. Phan, Y. Hong, and E. Viterbo, "Embedded delay-Doppler channel estimation for orthogonal time frequency space modulation," in *Proc. IEEE 88th Veh. Technol. Conf. (VTC-Fall)*, Aug. 2018, pp. 1–5.

[38] T. Thaj and E. Viterbo, "Low complexity iterative rake decision feedback equalizer for zero-padded OTFS systems," *IEEE Trans. Veh. Technol.*, vol. 69, no. 12, pp. 15606–15622, Dec. 2020.

[39] T. P. Zielinski, *Starting Digital Signal Processing in Telecommunication Engineering: A Laboratory-Based Course*. Cham, Switzerland: Springer, 2020.

[40] E. Aboutanios and S. Ye, "Efficient iterative estimation of the parameters of a damped complex exponential in noise," *IEEE Signal Process. Lett.*, vol. 21, no. 8, pp. 975–979, Aug. 2014.

[41] K. Duda, L. B. Magalas, M. Majewski, and T. P. Zielinski, "DFT-based estimation of damped oscillation parameters in low-frequency mechanical spectroscopy," *IEEE Trans. Instrum. Meas.*, vol. 60, no. 11, pp. 3608–3618, Nov. 2011.

[42] S. M. Kay, *Fundamentals of Statistical Signal Processing: Estimation Theory*. Englewood Cliffs, NJ, USA: Prentice-Hall, 1993.

[43] F. Colone, D. W. O'Hagan, P. Lombardo, and C. J. Baker, "A multistage processing algorithm for disturbance removal and target detection in passive bistatic radar," *IEEE Trans. Aerosp. Electron. Syst.*, vol. 45, no. 2, pp. 698–722, Apr. 2009.

[44] C. Schwark and D. Cristallini, "Advanced multipath clutter cancellation in OFDM-based passive radar systems," in *Proc. IEEE Radar Conf. (RadarConf)*, May 2016, pp. 1–4.

[45] M. Henninger, S. Mandelli, A. Grudnitsky, T. Wild, and S. ten Brink, "CRAP: Clutter removal with acquisitions under phase noise," 2023, *arXiv:2306.00598*.

[46] W. C. Barott and J. Engle, "Single-antenna ATSC passive radar observations with remodulation and keystone formatting," in *Proc. IEEE Radar Conf.*, May 2014, pp. 159–163.